# Microwave Tomographic Imaging of Cerebrovascular Accidents by Using High-Performance Computing

Pierre-Henri Tournier, Ioannis Aliferis, Marcella Bonazzoli, Maya de Buhan, Marion Darbas, Victorita Dolean, Frédéric Hecht, Pierre Jolivet, Ibtissam El Kanfoud, Claire Migliaccio, et al.

# Microwave Tomographic Imaging of Cerebrovascular Accidents by Using High-Performance Computing

P.-H. Tournier[a,b], I. Aliferis[c], M. Bonazzoli[d], M. de Buhan[e], M. Darbas[f], V. Dolean[d,g], F. Hecht[a,b], P. Jolivet[h], I. El Kanfoud[c], C. Migliaccio[c], F. Nataf[a,b], C. Pichot[c], S. Semenov[i]

[a]*Laboratoire Jacques-Louis Lions, UMR CNRS 7598, Sorbonne Universités, UPMC, Paris, France*
[b]*INRIA-Paris, EPC Alpines, Paris, France*
[c]*Laboratoire LEAT, UMR CNRS 7248, Université Nice Sophia Antipolis, Sophia Antipolis, France*
[d]*Laboratoire J.A. Dieudonné, UMR CNRS 7351, Université Nice Sophia Antipolis, Nice, France*
[e]*MAP5, UMR CNRS 8145, Université Paris-Descartes, Sorbonne Paris Cité, France*
[f]*LAMFA, UMR CNRS 7352, Université de Picardie Jules Verne, Amiens, France*
[g]*Dept of Maths and Stats, University of Strathclyde, Glasgow, UK*
[h]*IRIT, UMR CNRS 5505, Toulouse, France*
[i]*EMTensor GmbH, TechGate, 1220 Vienna, Austria*

**Abstract**

The motivation of this work is the detection of cerebrovascular accidents by microwave tomographic imaging. This requires the solution of an inverse problem relying on a minimization algorithm (for example, gradient-based), where successive iterations consist in repeated solutions of a direct problem. The reconstruction algorithm is extremely computationally intensive and makes use of efficient parallel algorithms and high-performance computing. The feasibility of this type of imaging is conditioned on one hand by an accurate reconstruction of the material properties of the propagation medium and on the other hand by a considerable reduction in simulation time. Fulfilling these two requirements will enable a very rapid and accurate diagnosis. From the mathematical and numerical point of view, this means solving Maxwell's equations in time-harmonic regime by appropriate domain decomposition methods, which are naturally adapted to parallel architectures.

*Keywords:* inverse problem, scalable preconditioners, Maxwell's equations, microwave imaging

## 1. Introduction

A stroke, also known as cerebrovascular accident, is a disturbance in the blood supply to the brain caused by a blocked or burst blood vessel. As a consequence, cerebral tissues are deprived of oxygen and nutrients. This results in a rapid loss of brain functions and often death. Strokes are classified into two major categories: ischemic (85% of strokes) and hemorrhagic (15% of strokes). During an acute ischemic stroke, the blood supply to a part of the brain is interrupted by thrombosis - the formation of a blood clot in a blood vessel - or by an embolism elsewhere in the body. A hemorrhagic stroke occurs when a blood vessel bursts inside the brain, increasing pressure in the brain and injuring brain cells. The two types of strokes result in opposite variations of the dielectric properties of the affected tissues. How quickly one can detect and characterize the stroke is of fundamental importance for the survival of the patient. The quicker the treatment is, the more reversible the damage and the better the chances of recovery are. Moreover, the treatment of ischemic stroke consists in thinning the blood (anticoagulants) and can be fatal if the stroke is hemorrhagic. Therefore, it is vital to make a clear distinction between the two types of strokes before treating the patient. Moreover, ideally one would want to monitor continuously the effect of the treatment on the evolution of the stroke during the hospitalization. The two most used imaging techniques for strokes diagnosis are MRI (magnetic resonance imaging) and CT scan (computerized tomography scan). One of their downsides is that the travel time from the patient's home to the hospital is lost. Moreover, the cost and the lack of portability of MRI and the harmful character of CT scan make them unsuitable for a continuous monitoring at the hospital during treatment.

This has motivated the study of an additional technique: microwave tomography. The measurement system is lightweight and thus transportable. The acquisition of the data is harmless and faster than CT or MRI. Hence, this imaging modality could be used by an emergency unit and for monitoring at the hospital. At frequencies of the order of 1 GHz, the tissues are well differentiated and can be imaged on the basis of their dielectric properties. After the first works on microwave imaging in 1982 by Lin and Clarke [1], other works followed, but almost always on synthetic simplified models [2]. New devices are currently designed and studied by EMTensor GmbH

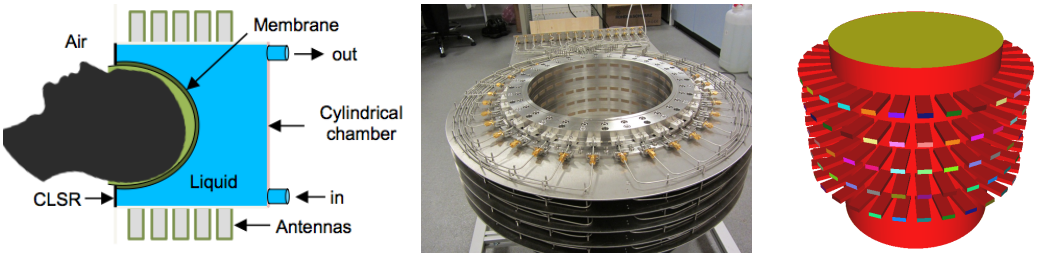


Figure 1: Left: Operating principle of the diagnosis apparatus. Middle: imaging chamber prototype of EMTensor, by courtesy of EMTensor company. Right: the corresponding simulation domain.

(Vienna, Austria) [3].

The purpose of this work is to solve in parallel the inverse problem associated with the time-harmonic Maxwell's equations which model electromagnetic waves propagation. The dielectric properties of the brain tissues of a patient yield the image that could be used for a rapid diagnosis of brain strokes. Simulation results presented in this work have been obtained on the imaging system prototype developed by EMTensor GmbH [3] (see Figure 1). It is composed of 5 rings of 32 ceramic-loaded rectangular waveguides around a metallic cylindrical chamber of diameter 28.5 cm and total height 28 cm. The head of the patient is inserted into the chamber as shown in Figure 1 (left). The imaging chamber is filled with a matching solution and a membrane is used to isolate the head. Each antenna successively transmits a signal at a fixed frequency, typically 1 GHz. The electromagnetic wave propagates inside the chamber and in the object to be imaged according to its electromagnetic properties. The retrieved data then consist in the scattering parameters measured by the 160 receiving antennas, which are used as input for the inverse problem. These raw data can be wirelessly transferred to a remote computing center. The HPC machine will then compute the 3D images of the patient's brain. Once formed, these images can be quickly transmitted from the computing center to the hospital, see Figure 2.

The paper is organized as follows. In Section 2 the direct problem and the time-harmonic Maxwell's equations in curl-curl form with suitable boundary conditions are introduced. In Section 3, we briefly describe the discretization method with edge finite elements. Section 4 is devoted to the introduction of the domain decomposition preconditioner. In Section 5 we explain how to compute the scattering coefficients. We also compare measurement data obtained by EMTensor with the coefficients computed by the simulation.

Figure 2: Design concept of the diagnosis technology, by courtesy of EMTensor company.

We introduce the inverse problem in Section 6. Section 7 is dedicated to numerical results. We first perform a strong scaling analysis to show the effectiveness of the domain decomposition method. Then, we present results obtained by solving the inverse problem in a realistic configuration, with noisy synthetic data generated using a numerical brain model with a simulated hemorrhagic stroke. Finally, we conclude this paper in Section 8 and give directions for future research.

## 2. The direct problem

Let the domain $\Omega \subset \mathbb{R}^3$ represent the imaging chamber (see Figure 1, right). We consider in $\Omega$ a heterogeneous non-magnetic dissipative linear isotropic dielectric medium, of dielectric permittivity $\varepsilon(\mathbf{x}) > 0$ and electrical conductivity $\sigma(\mathbf{x}) \geq 0$. For each transmitting antenna $j = 1, \ldots, N$ emitting a time periodic signal at angular frequency $\omega$, the complex amplitude $\mathbf{E}_j(\mathbf{x})$ of the associated electric field $\mathcal{E}_j(\mathbf{x}, \mathbf{t}) = \Re(\mathbf{E}_j(\mathbf{x})e^{\mathrm{i}\omega\mathbf{t}})$ is solution to the following second order time-harmonic Maxwell's equation:

$$\nabla \times (\nabla \times \mathbf{E}_j) - \mu_0(\omega^2\varepsilon - \mathrm{i}\omega\sigma)\mathbf{E}_j = 0 \quad \text{in } \Omega, \tag{1}$$

where $\mu_0$ is the permeability of free space. Note that the coefficient $\kappa = \mu_0(\omega^2\varepsilon - \mathrm{i}\omega\sigma)$ in the equation can be written as $\kappa = \omega^2\mu_0\big(\varepsilon - \mathrm{i}\frac{\sigma}{\omega}\big)$, and in the next sections we will consider the relative complex permittivity $\varepsilon_r$ given by the relation $\varepsilon_r\varepsilon_0 = \varepsilon - \mathrm{i}\frac{\sigma}{\omega}$, where $\varepsilon_0$ is the permittivity of free space. Let $\mathbf{n}$ be the unit outward normal to $\partial\Omega$. Equation (1) is equipped with perfectly conducting boundary conditions on the metallic walls $\Gamma_{\mathrm{m}}$:

$$\mathbf{E}_j \times \mathbf{n} = 0 \quad \text{on } \Gamma_{\mathrm{m}},$$

and with impedance boundary conditions on the outer section of the transmitting waveguide $j$ and of the receiving waveguides $i = 1, \ldots, N$, $i \neq j$ (see [4]):

$$(\nabla \times \mathbf{E}_j) \times \mathbf{n} + \mathrm{i}\beta \mathbf{n} \times (\mathbf{E}_j \times \mathbf{n}) = \mathbf{g}_j \quad \text{on } \Gamma_j, \tag{2}$$

$$(\nabla \times \mathbf{E}_j) \times \mathbf{n} + \mathrm{i}\beta \mathbf{n} \times (\mathbf{E}_j \times \mathbf{n}) = 0 \quad \text{on } \Gamma_i \ , \ i \neq j. \tag{3}$$

Here $\beta$ is the propagation wavenumber along the waveguide, corresponding to the propagation of the $\mathrm{TE}_{10}$ fundamental mode. Equation (2) imposes an incident wave which corresponds to the excitation of the fundamental mode $\mathbf{E}_j^0$ of the $j$-th waveguide, with $\mathbf{g}_j = (\nabla \times \mathbf{E}_j^0) \times \mathbf{n} + \mathrm{i}\beta \mathbf{n} \times (\mathbf{E}_j^0 \times \mathbf{n})$. On the other hand equation (3) corresponds to a first order absorbing boundary condition of Silver–Müller approximating a transparent boundary condition on the outer section of the receiving waveguides $i = 1, \ldots, N$, $i \neq j$. The bottom of the chamber is metallic, and we impose an impedance boundary condition on the top of the chamber. We end up with the following boundary value problem for each transmitting antenna $j = 1, \ldots, N$: find $\mathbf{E}_j$ such that

$$\begin{cases} \nabla \times (\nabla \times \mathbf{E}_j) - \mu_0(\omega^2 \varepsilon - \mathrm{i}\omega\sigma)\mathbf{E}_j = 0 & \text{in } \Omega, \\ \mathbf{E}_j \times \mathbf{n} = 0 & \text{on } \Gamma_{\mathrm{m}}, \\ (\nabla \times \mathbf{E}_j) \times \mathbf{n} + \mathrm{i}\beta \mathbf{n} \times (\mathbf{E}_j \times \mathbf{n}) = \mathbf{g}_j & \text{on } \Gamma_j, \\ (\nabla \times \mathbf{E}_j) \times \mathbf{n} + \mathrm{i}\beta \mathbf{n} \times (\mathbf{E}_j \times \mathbf{n}) = 0 & \text{on } \Gamma_i \ , \ i \neq j. \end{cases} \tag{4}$$

Now, let $V = \{\mathbf{v} \in H(\mathrm{curl}, \Omega), \mathbf{v} \times \mathbf{n} = 0 \text{ on } \Gamma_{\mathrm{m}}\}$, where $H(\mathrm{curl}, \Omega) = \{\mathbf{v} \in L_2(\Omega)^3, \nabla \times \mathbf{v} \in L_2(\Omega)^3\}$ is the space of square integrable functions whose curl is also square integrable. For each transmitting antenna $j = 1, \ldots, N$, the variational form of problem (4) reads: find $\mathbf{E}_j \in V$ such that

$$\begin{aligned} &\int_\Omega \left[ (\nabla \times \mathbf{E}_j) \cdot (\nabla \times \mathbf{v}) - \mu_0(\omega^2 \varepsilon - \mathrm{i}\omega\sigma)\mathbf{E}_j \cdot \mathbf{v} \right] \\ &+ \int_{\bigcup_{i=1}^N \Gamma_i} \mathrm{i}\beta (\mathbf{E}_j \times \mathbf{n}) \cdot (\mathbf{v} \times \mathbf{n}) = \int_{\Gamma_j} \mathbf{g}_j \cdot \mathbf{v} \quad \forall \mathbf{v} \in V. \end{aligned} \tag{5}$$

## 3. Edge finite elements

Nédélec edge elements [5] are finite elements particularly suited for the approximation of electromagnetic fields. Indeed, given a tetrahedral mesh $\mathcal{T}$ of the computational domain $\Omega$, the finite dimensional subspace $V_h$ generated

by Nédélec basis functions is included in $H(\mathrm{curl}, \Omega)$, since their tangential component across faces shared by adjacent tetrahedra of $\mathcal{T}$ is continuous. They thus match the continuity properties of the electric field. Nédélec elements are called edge elements because the basis functions are associated with the edges of the mesh $\mathcal{T}$. More precisely, for a tetrahedron $T \in \mathcal{T}$, the local basis functions are associated with the *oriented* edges $e = \{n_i, n_j\}$ of $T$ as follows

$$\mathbf{w}^e = \lambda_i \nabla \lambda_j - \lambda_j \nabla \lambda_i,$$

where the $\lambda_\ell$ are the barycentric coordinates of a point with respect to the node $n_\ell$ of $T$. Note that the polynomial degree of $\mathbf{w}^e$ is 1 since the barycentric coordinates $\lambda_\ell$ are polynomials of degree 1 and their gradients are constant. As these basis functions are vector functions, we only need one set of unknowns to approximate all the components of the field, and not three sets of unknowns, one for each component of the field as is instead required for usual nodal (scalar) finite elements.

The finite element discretization of the variational problem is obtained by taking test functions $\mathbf{v} \in V_h$, the edge finite element space on the mesh $\mathcal{T}$, and by looking for a solution $\mathbf{E}_h \in V_h$ in the same space: find $\mathbf{E}_h \in V_h$ such that

$$\begin{aligned} &\int_\Omega \left[ (\nabla \times \mathbf{E}_h) \cdot (\nabla \times \mathbf{v}) - \mu_0(\omega^2 \varepsilon - \mathrm{i}\omega\sigma) \mathbf{E}_h \cdot \mathbf{v} \right] \\ &+ \int_{\bigcup_{i=1}^N \Gamma_i} \mathrm{i}\beta (\mathbf{E}_h \times \mathbf{n}) \cdot (\mathbf{v} \times \mathbf{n}) = \int_{\Gamma_j} \mathbf{g}_j \cdot \mathbf{v} \quad \forall \mathbf{v} \in V_h. \end{aligned} \tag{6}$$

Locally, over each tetrahedron $T$, we write the discretized field as $\mathbf{E}_h = \sum_{e \in T} c_e \mathbf{w}^e$, a linear combination with coefficients $c_e$ of the basis functions associated with the edges $e$ of $T$, and the coefficients $c_e$ will be the unknowns of the resulting linear system. For edge finite elements (of degree 1) these coefficients can be interpreted as the *circulations* of $\mathbf{E}_h$ along the edges of the tetrahedra:

$$c_e = \frac{1}{|e|} \int_e \mathbf{E}_h \cdot \mathbf{t}_e,$$

where $\mathbf{t}_e$ is the tangent vector to the edge $e$ of length $|e|$, the length of $e$. This is a consequence of the fact that the basis functions are in duality with the *degrees of freedom* given by the circulations along the edges, that is:

$$\frac{1}{|e|} \int_e \mathbf{w}^{e'} \cdot \mathbf{t}_e = \begin{cases} 1 & \text{if } e = e', \\ 0 & \text{if } e \neq e'. \end{cases}$$

## 4. Domain decomposition preconditioning

The finite element discretization (6) of the variational problem (5) produces linear systems

$$A\mathbf{u}_j = \mathbf{b}_j$$

for each transmitting antenna $j$. However, the matrix $A$ can be ill-conditioned. This, combined with the fact that the underlying PDE is indefinite, highlights the need for a robust and efficient preconditioner. Here we employ domain decomposition preconditioners, which are extensively described in [6], as they are naturally suited to parallel computing. Our domain decomposition preconditioner is presented in the following.

Let $\mathcal{T}$ be the mesh of the computational domain $\Omega$. First, $\mathcal{T}$ is partitioned into $N_S$ non-overlapping meshes $\{\mathcal{T}_i\}_{1\leqslant i\leqslant N_S}$ using standard graph partitioners such as SCOTCH [7] or METIS [8]. If $\delta$ is a positive integer, the *overlapping* decomposition $\{\mathcal{T}_i^\delta\}_{1\leqslant i\leqslant N_S}$ is defined recursively as follows: $\mathcal{T}_i^\delta$ is obtained by including all tetrahedra of $\mathcal{T}_i^{\delta-1}$ plus all adjacent tetrahedra of $\mathcal{T}_i^{\delta-1}$; for $\delta = 0$, $\mathcal{T}_i^\delta = \mathcal{T}_i$. Note that the number of layers in the overlap is then $2\delta$. Let $V_h$ be the edge finite element space defined on $\mathcal{T}$, and $\{V_i^\delta\}_{1\leqslant i\leqslant N_S}$ the local edge finite element spaces defined on $\{\mathcal{T}_i^\delta\}_{1\leqslant i\leqslant N_S}$, $\delta > 0$. Now consider the restrictions $\{R_i\}_{1\leqslant i\leqslant N_S}$ from $V_h$ to $\{V_i^\delta\}_{1\leqslant i\leqslant N_S}$, and a local partition of unity $\{D_i\}_{1\leqslant i\leqslant N_S}$ such that

$$\sum_{i=1}^{N_S} R_i^T D_i R_i = I_{n\times n}. \tag{7}$$

Algebraically speaking, if $n$ is the global number of unknowns and $\{n_i\}_{1\leqslant i\leqslant N_S}$ are the numbers of unknowns for each local finite element space, then $R_i$ is a Boolean matrix of size $n_i \times n$, and $D_i$ is a diagonal matrix of size $n_i \times n_i$, for all $1 \leqslant i \leqslant N_S$. Note that $R_i^T$, the transpose of $R_i$, is a $n \times n_i$ matrix that gives the extension by 0 from $V_i^\delta$ to $V_h$.

Using these matrices, one can define the following one-level preconditioner, called Optimized Restricted Additive Schwarz preconditioner (ORAS) [9]:

$$M_{\text{ORAS}}^{-1} = \sum_{i=1}^{N_S} R_i^T D_i B_i^{-1} R_i, \tag{8}$$

where $\{B_i\}_{1\leqslant i\leqslant N_S}$ are local operators corresponding to the subproblems with impedance boundary conditions $(\nabla \times \mathbf{E}) \times \mathbf{n} + \mathtt{i}k\mathbf{n} \times (\mathbf{E} \times \mathbf{n})$, where $k = \omega\sqrt{\mu_0\varepsilon_r\varepsilon_0}$ is the wavenumber. These boundary conditions were first used as

transmission conditions at the interfaces between subdomains in [10]. The local matrices $\{B_i\}_{1\leqslant i\leqslant N_S}$ of the ORAS preconditioner make use of more efficient transmission boundary conditions than the submatrices $\{R_i A R_i^T\}_{1\leqslant i\leqslant N_S}$ of the original Restricted Additive Schwarz (RAS) preconditioner [11]. It is important to note that when a direct solver is used to compute the action of $B_i^{-1}$ on multiple vectors, it can be done in a single forward elimination and backward substitution. More details on the solution of linear systems with multiple right-hand sides are given in Section 7. The preconditioner $M_{\text{ORAS}}^{-1}$ (8) is naturally parallel since its assembly requires the concurrent factorization of each $\{B_i\}_{1\leqslant i\leqslant N_S}$, which are typically stored locally on different processes in a distributed computing context. Likewise, applying (8) to a distributed vector only requires peer-to-peer communications between neighboring subdomains, and a local forward elimination and backward substitution. See chapter 8 of [6] for a more detailed analysis.

### *4.1. Partition of unity*

The construction of the partition of unity is intricate, especially for Nédélec edge finite elements.

The starting point is the construction of partition of unity functions $\{\chi_i\}_{1\leqslant i\leqslant N_S}$ for the classical P1 linear nodal finite element, whose degrees of freedom are the values at the nodes of the mesh. First of all, we define for $i = 1, \ldots, N_S$ the function $\widetilde{\chi}_i$ as the continuous piecewise linear function on $\mathcal{T}$, with support contained in $\mathcal{T}_i^\delta$, such that

$$\widetilde{\chi}_i = \begin{cases} 1 & \text{at all nodes of } \mathcal{T}_i^0, \\ 0 & \text{at all nodes of } \mathcal{T}_i^\delta \setminus \mathcal{T}_i^0. \end{cases}$$

The function $\chi_i$ can then be defined as the continuous piecewise linear function on $\mathcal{T}$, with support contained in $\mathcal{T}_i^\delta$, such that its (discrete) value for each degree of freedom is evaluated by:

$$\chi_i = \frac{\widetilde{\chi}_i}{\sum_{j=1}^{N_S} \widetilde{\chi}_j}. \tag{9}$$

Thus, we have $\sum_{i=1}^{N_S} \chi_i = \mathbf{1}$ both at the discrete and continuous level. Remark that if $\delta > 1$, not only the function $\chi_i$ but also its derivative is equal to zero on the border of $\mathcal{T}_i^\delta$. This is essential for a good convergence if Robin boundary

conditions are chosen as transmission conditions at the interfaces between subdomains. Indeed, if this property is satisfied, the continuous version of the ORAS algorithm is equivalent to P. L. Lions' algorithm (see [9] and [6] §2.3.2). Note that in the practical implementation, the functions $\widetilde{\chi}_i$ and $\chi_i$ are constructed locally on $\mathcal{T}_i^\delta$, the relevant contribution of the $\widetilde{\chi}_j$ in (9) being on $\mathcal{T}_j^\delta \cap \mathcal{T}_i^\delta$. This removes all dependency on the global mesh $\mathcal{T}$, which could be otherwise problematic at large scales.

Now, the degrees of freedom of Nédélec finite elements are associated with the edges of the mesh. For these finite elements, we can build a geometric partition of unity based on the support of the degrees of freedom (the edges of the mesh): the entries of the diagonal matrices $D_i$, $i = 1, \ldots, N_S$ are obtained for each degree of freedom by interpolating the piecewise linear function $\chi_i$ at the midpoint of the corresponding edge. The partition of unity property (7) is then satisfied since $\sum_{i=1}^{N_S} \chi_i = \mathbf{1}$.

### *4.2. Software stack*

All operators related to the domain decomposition method can be easily generated using finite element Domain-Specific Languages (DSL). Here we use FreeFem++ [12] (`http://www.freefem.org/ff++/`) since it has already been proven that it can enable large-scale simulations using overlapping Schwarz methods [13] when used in combination with the library HPDDM [14] (High-Performance unified framework for Domain Decomposition Methods, `https://github.com/hpddm/hpddm`). HPDDM implements several domain decomposition methods such as RAS, ORAS, FETI, and BNN. It uses multiple levels of parallelism: communication between subdomains is based on the Message Passing Interface (MPI), and computations in the subdomains can be executed on several threads by calling optimized BLAS libraries (such as Intel MKL), or shared-memory direct solvers like PARDISO. Domain decomposition methods naturally offer good parallel properties on distributed architectures. The computational domain is decomposed into subdomains in which concurrent computations are performed. The coupling between subdomains requires communications between computing nodes via messages. The strong scalability of the ORAS preconditioner as implemented in HPDDM for the direct problem presented in Section 2 will be assessed in Section 7.

## 5. Computing the scattering parameters

In order to compute the numerical counterparts of the *reflection and transmission coefficients* obtained by the measurement apparatus of the imaging chamber shown in Figure 1, we use the following formula, which is appropriate in the case of open-ended waveguides:

$$S_{ij} = \frac{\displaystyle\int_{\Gamma_i} \overline{\mathbf{E}_j} \cdot \mathbf{E}_i^0}{\displaystyle\int_{\Gamma_i} |\mathbf{E}_i^0|^2}, \quad i, j = 1, \ldots, N, \tag{10}$$

where $\mathbf{E}_i^0$ is the $\mathrm{TE}_{10}$ fundamental mode of the $i$-th receiving waveguide and $\mathbf{E}_j$ is the solution of the problem where the $j$-th waveguide transmits the signal ($\overline{\mathbf{E}_j}$ denotes the complex conjugate of $\mathbf{E}_j$). The $S_{ij}$ with $i \neq j$ are the transmission coefficients, and the $S_{jj}$ are the reflection coefficients. They are gathered in the scattering matrix, also called S-matrix.

Here we compare the coefficients computed from the simulation with a set of measurements obtained by EMTensor. For this test case, the imaging chamber was filled with a homogeneous matching solution. The electric permittivity $\varepsilon$ of the matching solution is chosen by EMTensor in order to minimize contrasts with the ceramic-loaded waveguides and with the different brain tissues. The choice of the conductivity $\sigma$ of the matching solution is a compromise between the minimization of reflection artifacts from metallic boundaries and the desire to have best possible signal-to-noise ratio. Here the relative complex permittivity of the matching solution at frequency $f = 1\,\mathrm{GHz}$ is $\varepsilon_r^{\mathrm{gel}} = 44 - 20\mathtt{i}$. The relative complex permittivity inside the ceramic-loaded waveguides is $\varepsilon_r^{\mathrm{cer}} = 59$.

The set of experimental data at hand given by EMTensor consists in transmission coefficients for transmitting antennas in the second ring from the top. Figure 3 shows the normalized magnitude (dB) and phase (degree) of the complex coefficients $S_{ij}$ corresponding to a transmitting antenna in the second ring from the top and to the 31 receiving antennas in the middle ring (note that measured coefficients are available only for 17 receiving antennas). The magnitude in dB is calculated as $20 \log_{10}(|S_{ij}|)$. The normalization is done by dividing every transmission coefficient by the transmission coefficient corresponding to the receiving antenna directly opposite to the transmitting antenna, which is thus set to 1. Since we normalize with respect to the coefficient having the lowest expected magnitude, the magnitude

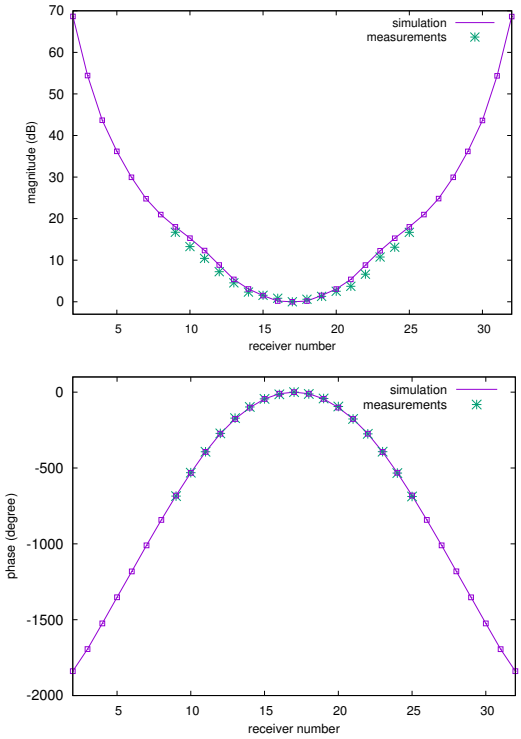


Figure 3: The normalized magnitude (top) and phase (bottom) of the transmission coefficients computed with the simulation and measured experimentally.

of the transmission coefficients displayed in Figure 3 is larger than 0 dB. We can see that the transmission coefficients computed from the simulation are in very good agreement with the measurements.

## 6. The inverse problem

The inverse problem that we consider consists in finding the unknown dielectric permittivity $\varepsilon(\mathbf{x})$ and conductivity $\sigma(\mathbf{x})$ in $\Omega$, such that the solutions $\mathbf{E}_j, j = 1, \ldots, N$ of problem (4) lead to corresponding scattering parameters $S_{ij}$ (10) that coincide with the measured scattering parameters $S_{ij}^{\text{mes}}$, for $i, j = 1, \ldots, N$. In the following, we present the inverse problem in the continuous setting for clarity.

Let $\kappa = \mu_0(\omega^2\varepsilon - \mathrm{i}\omega\sigma)$ be the unknown complex parameter of our inverse problem, and let us denote by $\mathbf{E}_j(\kappa)$ the solution of the direct problem (4) with dielectric permittivity $\varepsilon$ and conductivity $\sigma$. The corresponding

scattering parameters will be denoted by $S_{ij}(\kappa)$ for $i,j=1,\dots,N$:

$$S_{ij}(\kappa)=\frac{\displaystyle\int_{\Gamma_i}\overline{\mathbf{E}_j(\kappa)}\cdot\mathbf{E}_i^0}{\displaystyle\int_{\Gamma_i}|\mathbf{E}_i^0|^2},\quad i,j=1,\dots,N.$$

The misfit of the parameter $\kappa$ to the data can be defined through the following functional:

$$J(\kappa)=\frac{1}{2}\sum_{j=1}^{N}\sum_{i=1}^{N}\left|S_{ij}(\kappa)-S_{ij}^{\mathrm{mes}}\right|^2=\frac{1}{2}\sum_{j=1}^{N}\sum_{i=1}^{N}\left|\frac{\displaystyle\int_{\Gamma_i}\overline{\mathbf{E}_j(\kappa)}\cdot\mathbf{E}_i^0}{\displaystyle\int_{\Gamma_i}|\mathbf{E}_i^0|^2}-S_{ij}^{\mathrm{mes}}\right|^2. \tag{11}$$

In a classical way, solving the inverse problem then consists in minimizing the functional $J$ with respect to the parameter $\kappa$. Computing the differential of $J$ in a given arbitrary direction $\delta\kappa$ yields

$$DJ(\kappa,\delta\kappa)=\sum_{j=1}^{N}\sum_{i=1}^{N}\Re\left[\overline{\left(S_{ij}(\kappa)-S_{ij}^{\mathrm{mes}}\right)}\frac{\displaystyle\int_{\Gamma_i}\overline{\delta\mathbf{E}_j(\kappa)}\cdot\mathbf{E}_i^0}{\displaystyle\int_{\Gamma_i}|\mathbf{E}_i^0|^2}\right],\quad \delta\kappa\in\mathbb{C},$$

where $\delta\mathbf{E}_j(\kappa)$ is the solution of the following linearized problem:

$$\begin{cases}\nabla\times(\nabla\times\delta\mathbf{E}_j)-\kappa\delta\mathbf{E}_j=\delta\kappa\mathbf{E}_j & \text{in } \Omega,\\ \delta\mathbf{E}_j\times\mathbf{n}=0 & \text{on } \Gamma_{\mathrm{m}},\\ (\nabla\times\delta\mathbf{E}_j)\times\mathbf{n}+\mathrm{i}\beta\mathbf{n}\times(\delta\mathbf{E}_j\times\mathbf{n})=0 & \text{on } \Gamma_i\ ,\ i=1,\dots,N.\end{cases} \tag{12}$$

We now use the adjoint approach in order to simplify the expression of $DJ$. This will allow us to compute the gradient efficiently after discretization, with a number of computations independent of the size of the parameter space. Considering the variational formulation of problem (12) with a test

function $\mathbf{F}$ and integrating by parts, we get

$$\begin{aligned}\int_\Omega \delta\kappa \mathbf{E}_j \cdot \mathbf{F} &= \int_\Omega (\nabla \times (\nabla \times \delta\mathbf{E}_j) - \kappa \delta\mathbf{E}_j) \cdot \mathbf{F} \\ &= \int_\Omega (\nabla \times (\nabla \times \mathbf{F}) - \kappa \mathbf{F}) \cdot \delta\mathbf{E}_j - \int_{\partial\Omega} ((\nabla \times \delta\mathbf{E}_j) \times \mathbf{n}) \cdot \mathbf{F} \\ &+ \int_{\partial\Omega} ((\nabla \times \mathbf{F}) \times \mathbf{n}) \cdot \delta\mathbf{E}_j \\ &= \int_\Omega (\nabla \times (\nabla \times \mathbf{F}) - \kappa \mathbf{F}) \cdot \delta\mathbf{E}_j + \sum_{i=1}^{N} \int_{\Gamma_i} \mathrm{i}\beta (\mathbf{n} \times (\mathbf{F} \times \mathbf{n})) \cdot \delta\mathbf{E}_j \\ &+ \int_{\Gamma_\mathrm{m}} (\nabla \times \delta\mathbf{E}_j) \cdot (\mathbf{F} \times \mathbf{n}) + \sum_{i=1}^{N} \int_{\Gamma_i} ((\nabla \times \mathbf{F}) \times \mathbf{n}) \cdot \delta\mathbf{E}_j.\end{aligned}$$

Introducing the solution $\mathbf{F}_j(\kappa)$ of the following adjoint problem

$$\begin{cases} \nabla \times (\nabla \times \mathbf{F}_j) - \kappa \mathbf{F}_j = 0 & \text{in } \Omega, \\ \mathbf{F}_j \times \mathbf{n} = 0 & \text{on } \Gamma_\mathrm{m}, \\ (\nabla \times \mathbf{F}_j) \times \mathbf{n} + \mathrm{i}\beta \mathbf{n} \times (\mathbf{F}_j \times \mathbf{n}) = \dfrac{(S_{ij}(\kappa) - S_{ij}^{\mathrm{mes}})}{\displaystyle\int_{\Gamma_i} |\mathbf{E}_i^0|^2} \overline{\mathbf{E}_i^0} & \text{on } \Gamma_i \ , \ i = 1, \ldots, N, \end{cases} \tag{13}$$

we get

$$\int_\Omega \delta\kappa \mathbf{E}_j \cdot \mathbf{F}_j = \sum_{i=1}^{N} (S_{ij}(\kappa) - S_{ij}^{\mathrm{mes}}) \frac{\displaystyle\int_{\Gamma_i} \overline{\mathbf{E}_i^0} \cdot \delta\mathbf{E}_j}{\displaystyle\int_{\Gamma_i} |\mathbf{E}_i^0|^2}.$$

Finally, the differential of $J$ can be computed as

$$DJ(\kappa, \delta\kappa) = \sum_{j=1}^{N} \Re \left[ \int_\Omega \overline{\delta\kappa \, \mathbf{E}_j \cdot \mathbf{F}_j} \right].$$

We can then compute the gradient to use in a gradient-based local optimization algorithm. The numerical results presented in Section 7 are obtained using a limited-memory Broyden-Fletcher-Goldfarb-Shanno (L-BFGS) algorithm. Note that every evaluation of $J$ requires the solution of the state problem (4) while the computation of the gradient requires the solution of (4)

as well as the solution of the adjoint problem (13). Moreover, the state and adjoint problems use the same operator. Therefore, the computation of the gradient only needs the assembly of one matrix and its associated domain decomposition preconditioner.

Numerical results for the reconstruction of a hemorrhagic stroke from synthetic data are presented in the next section. The functional $J$ considered in the numerical results is slightly different from (11), as we add a normalization term for each pair $(i, j)$ as well as a Tikhonov regularizing term:

$$J(\kappa) = \frac{1}{2} \sum_{j=1}^{N} \sum_{i=1}^{N} \frac{\left| S_{ij}(\kappa) - S_{ij}^{\text{mes}} \right|^2}{\left| S_{ij}^{\text{empty}} \right|^2} + \frac{\alpha}{2} \int_{\Omega} |\nabla \kappa|^2, \tag{14}$$

where $S_{ij}^{\text{empty}}$ refers to the coefficients computed from the simulation with the empty chamber, that is the chamber filled only with the homogeneous matching solution as described in the previous section, with no object inside. In this way, the contribution of each pair $(i, j)$ in the misfit functional is normalized and does not depend on the amplitude of the coefficient, which can vary greatly between pairs $(i, j)$ as displayed in Figure 3. The Tikhonov regularizing term aims at reducing the effects of noise in the data. For now, the regularization parameter $\alpha$ is chosen empirically so as to obtain a visually good compromise between reducing the effects of noise and keeping the reconstructed image pertinent. All calculations carried out in this section can be accommodated in a straightforward manner to definition (14) of the functional.

As is usually the case with most medical imaging techniques, the reconstruction is done layer by layer. For the imaging chamber of EMTensor that we study in this paper, one layer corresponds to one of the five rings of 32 antennas. This allows us to exhibit another level of parallelism, by solving an inverse problem independently for each of the five rings in parallel. More precisely, each of these inverse problems is solved in a domain truncated around the corresponding ring of antennas, containing at most two other rings (one ring above and one ring below). We impose absorbing boundary conditions on the artificial boundaries of the truncated computational domain. For each inverse problem, only the coefficients $S_{ij}$ with transmitting antennas $j$ in the corresponding ring are taken into account: we consider 32 antennas as transmitters and at most 96 antennas as receivers.

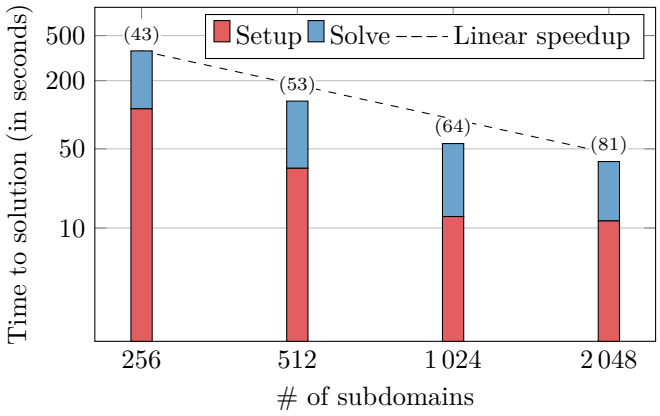


Figure 4: Strong scaling experiment. Colors indicate the fraction of the total time spent in the setup and solution phases. The number of GMRES iterations is reported in parentheses.

## 7. Numerical results

Results in this paper were obtained on Curie, a system composed of 5,040 nodes made of two eight-core Intel Sandy Bridge processors clocked at 2.7 GHz. The interconnect is an InfiniBand QDR full fat tree and the MPI implementation used was BullxMPI version 1.2.8.4. Intel compilers and Math Kernel Library in their version 16.0.2.181 were used for all binaries and shared libraries, and as the linear algebra backend for dense computations. One-level preconditioners such as (8) assembled by HPDDM require the use of a sparse direct solver. In the following experiments, we have been using either PARDISO [15] from Intel MKL or MUMPS [16]. All linear systems resulting from the edge finite elements discretization are solved by GMRES right-preconditioned with ORAS (8) as implemented in HPDDM. The GMRES algorithm is stopped once the unpreconditioned relative residual is lower than $10^{-8}$. First, we perform a strong scaling analysis in order to assess the efficiency of our preconditioner. We then solve the inverse problem in a realistic configuration, with noisy synthetic data generated using a numerical brain model with a simulated hemorrhagic stroke.

### *7.1. Scaling analysis*

Using the domain decomposition preconditioner (8), we solve the direct problem corresponding to the setting of Section 5 where the chamber is filled

| $N_S$ | Setup | Solve | # of iterations | Speedup |
|---|---|---|---|---|
| 256 | 293.36 | 73.06 | 43 | 1 |
| 512 | 95.11 | 36.92 | 53 | 2.8 |
| 1,024 | 35.13 | 20.55 | 64 | 6.6 |
| 2,048 | 25.89 | 12.77 | 81 | 9.5 |

Figure 5: Strong scaling experiment. Timings (in seconds) of the setup and solution phases.

with a homogeneous matching solution. We consider a right-hand side corresponding to a transmitting antenna in the second ring from the top. Given a fine mesh of the domain composed of 82 million tetrahedra, we increase the number of MPI processes to solve the linear system of 96 million double-precision complex unknowns yielded by the discretization of Maxwell's equation using edge elements. The global unstructured mesh is partitioned using SCOTCH [7] and the local solver is PARDISO from Intel MKL. We use one subdomain and two OpenMP threads per MPI process. Results are reported in Figure 5 and illustrated in Figure 4 with a plot of the time to solution including both the setup and solution phases on 256 up to 2048 subdomains. The setup time corresponds to the maximum time spent for the factorization of the local subproblem matrix $B_i$ in (8) over all subdomains, while the solution time corresponds to the time needed to solve the linear system with GMRES. We are able to obtain very good speedups up to 4096 cores (2048 subdomains) on Curie, with a superlinear speedup of 9.5 between 256 and 2048 subdomains.

### *7.2. Reconstruction of a hemorrhagic stroke from synthetic data*

In this subsection, we assess the feasibility of the microwave imaging technique presented in this paper for stroke detection and monitoring through a numerical example in a realistic configuration. We use synthetic data corresponding to a numerical model of a virtual human head with a simulated hemorrhagic stroke as input for the inverse problem. The numerical model of the virtual head comes from CT and MRI tomographic images and consists of a complex permittivity map of $362 \times 434 \times 362$ data points. Figure 6 (left) shows a sagittal section of the head. In the simulation, the head is immersed in the imaging chamber as shown in Figure 6 (right). In order to simulate a hemorrhagic stroke, a synthetic stroke is added in the form of an ellipsoid in which the value of the complex permittivity $\varepsilon_r$ has been increased. For this

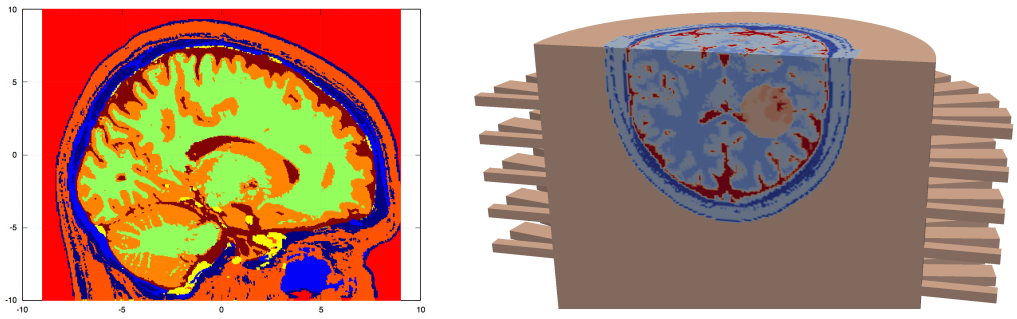

Figure 6: Left: sagittal section of the brain. Right: numerical head immersed in the imaging chamber, with a simulated ellipsoid-shaped hemorrhagic stroke.

test case, the value of the permittivity in the ellipsoid is taken as the mean value between the relative permittivity of the original healthy brain and the relative permittivity of blood at frequency $f = 1\,\mathrm{GHz}$, $\varepsilon_r^{\mathrm{blood}} = 68 - 44\mathrm{i}$. The imaging chamber is filled with a matching solution. The relative permittivity of the matching solution is chosen by EMTensor as explained in Section 5 and is equal to $\varepsilon_r^{\mathrm{gel}} = 44 - 20\mathrm{i}$ at frequency $f = 1\,\mathrm{GHz}$. In the real setting, a special membrane fitting the shape of the head is used in order to isolate the head from the matching medium. We do not take this membrane into account in this synthetic test case. The synthetic data are obtained by solving the direct problem on a mesh composed of 17.6 million tetrahedra (corresponding to approximately 20 points per wavelength) and consist in the transmission and reflection coefficients $S_{ij}$ calculated from the simulated electric field as in (10). We subsequently add noise to the real and imaginary parts of the coefficients $S_{ij}$ (10% additive Gaussian white noise, with different values for real and imaginary parts). The noisy data are then used as input for the inverse problem. Furthermore, we assume no a priori knowledge on the input data, and we set the initial guess for the inverse problem as the homogeneous matching solution everywhere inside the chamber. We use a piecewise linear approximation of the unknown parameter $\kappa$, defined on the same mesh used to solve the state and adjoint problems. For the purpose of parallel computations, the partitioning introduced by the domain decomposition method is also used to compute and store locally in each subdomain every entity involved in the inverse problem, such as the parameter $\kappa$ and the gradient.

Figure 7 shows the imaginary part of the exact and reconstructed permittivity for three steps of the evolution of the hemorrhagic stroke, from the

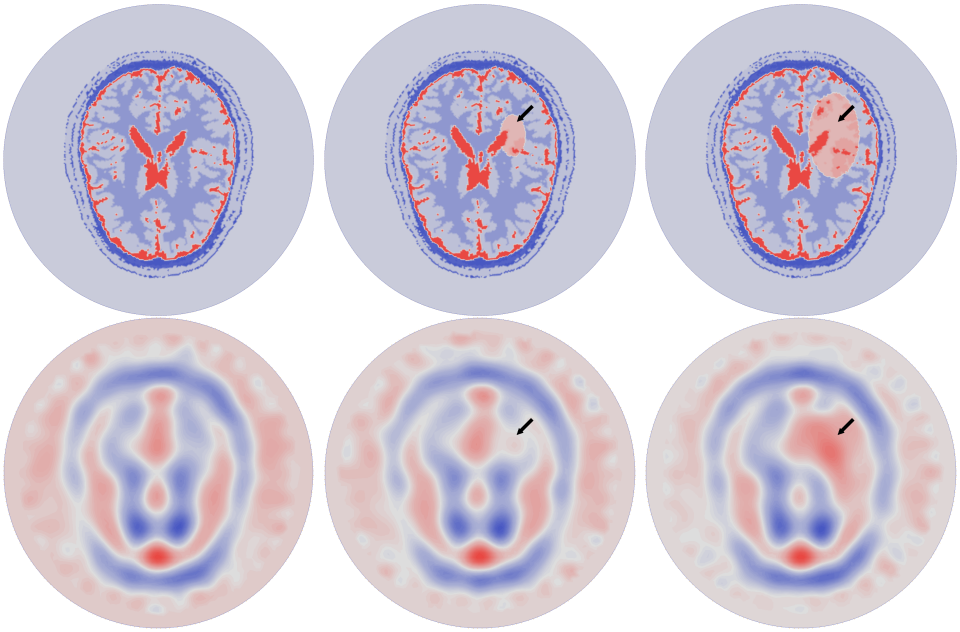

Figure 7: Top row: imaginary part of the exact permittivity used to produce noisy data as input for the inverse problem during time evolution of a simulated hemorrhagic stroke (indicated by the black arrow). The size of the ellipsoid is $3.9\,\mathrm{cm} \times 2.3\,\mathrm{cm} \times 2.3\,\mathrm{cm}$ and $7.7\,\mathrm{cm} \times 4.6\,\mathrm{cm} \times 4.6\,\mathrm{cm}$ in the middle and right column respectively. Bottom row: corresponding reconstructions obtained by taking into account only the first ring of transmitting antennas.

healthy brain (left column) to the large stroke (right column). Increasing the size of the ellipsoid in which the value of the permittivity is raised simulates the evolution of the stroke. Each of the three reconstructions in Figure 7 corresponds to the solution of an inverse problem in the truncated domain containing only the first two rings of antennas from the top, and where only the coefficients $S_{ij}$ corresponding to transmitting antennas $j$ in the first ring are taken into account. Each reconstruction starts from an initial guess consisting of the homogeneous matching solution and is obtained after reaching a convergence criterion of $10^{-2}$ for the value of the cost functional, which takes around 30 iterations of the L-BFGS algorithm.

Figure 8 gathers the results of a strong scaling experiment which consists in solving the same inverse problem corresponding to the third reconstructed image of Figure 7 for an increasing number of MPI processes. We report the total computing time needed to obtain the reconstructed image. For this

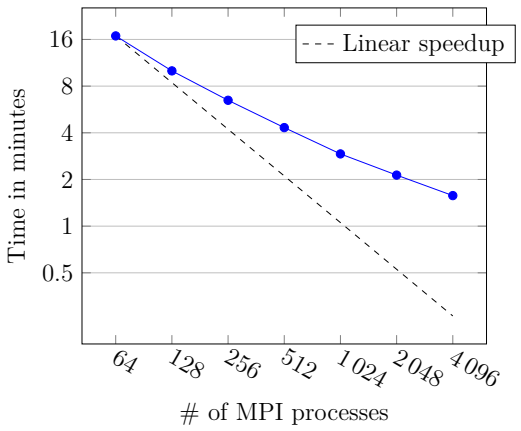


Figure 8: Strong scaling experiment: total time needed to obtain the third reconstructed image shown in Figure 7.

experiment we use one subdomain and one OpenMP thread per MPI process. The mesh of the computational domain is composed of 674 580 tetrahedra, corresponding to approximately 10 points per wavelength.

Note that evaluating the functional or its gradient requires the solution of a linear system with 32 right-hand sides, one right-hand side per transmitter. This introduces a trivial level of parallelism since the solution corresponding to each right-hand side can be computed independently. However when considering a finite number of available processors, there is a tradeoff between the parallelism induced by the multiple right-hand sides and the parallelism induced by the domain decomposition method. Additionally, we solve for multiple right-hand sides simultaneously using a pseudo-block method implemented inside GMRES which consists in fusing the multiple arithmetic operations corresponding to each right-hand side (matrix-vector products, dot products), resulting in higher arithmetic intensity. The scaling behavior of this pseudo-block algorithm with respect to the number of right-hand sides is nonlinear, as is the scaling behavior of the domain decomposition method with respect to the number of subdomains. Thus, for a given number of processors, we find the optimal tradeoff between parallelizing with respect to the number of subdomains or right-hand sides through trial and error. For example, the best computing time for 2048 MPI processes is achieved by using 8 domain decomposition communicators (i.e. 8 concurrent direct solves) with 256 subdomains treating 4 right-hand sides each.

Figure 8 shows that we can generate an image with a total computing

time of less than 2 minutes (94 seconds) using 4096 cores of Curie. These preliminary results are very encouraging as we are already able to achieve a satisfactory reconstruction time in the perspective of using such an imaging technique for monitoring. This allows clinicians to obtain almost instantaneous images 24/7 or on demand. Although the reconstructed images do not feature the complex heterogeneities of the brain, which is in accordance with what we expect from microwave imaging methods, they allow the characterization of the stroke and its monitoring.

## 8. Conclusion

We have developed a tool that reconstructs a microwave tomographic image of the brain in less than 2 minutes using 4096 cores. This computational time corresponds to clinician acceptance for rapid diagnosis or medical monitoring at the hospital. These images were obtained from noisy synthetic data from a very accurate model of the brain. To our knowledge, this is the first time that such a realistic study (operational acquisition device, highly accurate three-dimensional synthetic data, 10% noise) shows the feasibility of microwave imaging. This study was made possible by the use of massively parallel computers and facilitated by the HPDDM and FreeFem++ tools that we have developed. The next step is the validation of these results on clinical data.

Regarding the numerical aspects of this work, we will accelerate the solution of the series of direct problems, which accounts for more than 80% of our elapsed time. We explain here the three main avenues of research:

- The present ORAS solver for Maxwell's equations is a one level algorithm, which cannot scale well over thousands of subdomains. The introduction of a two-level preconditioner with an adequate coarse space would allow for very good speedups even for decompositions into a large number of subdomains.

- Recycling information obtained during the convergence of the optimization algorithm will also enable us to improve the performance of the method, see [17].

- Iterative block methods that allow for simultaneous solutions of linear systems have not been fully investigated. Arithmetic intensity would be increased since block methods may converge in a smaller number of iterations while exploiting modern computer architectures effectively.

**Acknowledgments**

This work was granted access to the HPC resources of TGCC@CEA under the allocations 2016-067519 and 2016-067730 made by GENCI. This work has been supported in part by ANR through project MEDIMAX, ANR-13-MONU-0012.

[1] J. C. Lin, M. J. Clarke, Microwave imaging of cerebral edema, Proceedings of the IEEE 70 (5) (1982) 523–524.

[2] S. Y. Semenov, D. R. Corfield, Microwave tomography for brain imaging: feasibility assessment for stroke detection, International Journal of Antennas and Propagation.

[3] S. Semenov, B. Seiser, E. Stoegmann, E. Auff, Electromagnetic tomography for brain imaging: from virtual to human brain, in: 2014 IEEE Conference on Antenna Measurements & Applications (CAMA), 2014.

[4] R. Beck, R. Hiptmair, Multilevel solution of the time-harmonic Maxwell's equations based on edge elements, International Journal for Numerical Methods in Engineering 45 (7) (1999) 901–920.

[5] J.-C. Nédélec, Mixed finite elements in $\mathbf{R}^3$, Numerische Mathematik 35 (3) (1980) 315–341.

[6] V. Dolean, P. Jolivet, F. Nataf, An Introduction to Domain Decomposition Methods: algorithms, theory and parallel implementation, SIAM, 2015.

[7] F. Pellegrini, J. Roman, SCOTCH: A Software Package for Static Mapping by Dual Recursive Bipartitioning of Process and Architecture Graphs, in: High-Performance Computing and Networking, Springer, 1996, pp. 493–498.

[8] G. Karypis, V. Kumar, A fast and high quality multilevel scheme for partitioning irregular graphs, SIAM Journal on Scientific Computing 20 (1) (1998) 359–392.

[9] A. St-Cyr, M. J. Gander, S. J. Thomas, Optimized multiplicative, additive, and restricted additive Schwarz preconditioning, SIAM Journal on Scientific Computing 29 (6) (2007) 2402–2425).

[10] B. Després, P. Joly, J. E. Roberts, A domain decomposition method for the harmonic Maxwell equations, in: Iterative methods in linear algebra (Brussels, 1991), North-Holland, Amsterdam, 1992, pp. 475–484.

[11] X.-C. Cai, M. Sarkis, A restricted additive Schwarz preconditioner for general sparse linear systems, SIAM Journal on Scientific Computing 21 (2) (1999) 792–797.

[12] F. Hecht, New development in FreeFem++, Journal of Numerical Mathematics 20 (3-4) (2012) 251–265.

[13] P. Jolivet, V. Dolean, F. Hecht, F. Nataf, C. Prud'homme, N. Spillane, High-performance domain decomposition methods on massively parallel architectures with FreeFem++, Journal of Numerical Mathematics 20 (3-4) (2012) 287–302.

[14] P. Jolivet, F. Hecht, F. Nataf, C. Prud'homme, Scalable domain decomposition preconditioners for heterogeneous elliptic problems, in: Proc. of the Int. Conference on High Performance Computing, Networking, Storage and Analysis, IEEE, 2013, pp. 1–11.

[15] O. Schenk, K. Gärtner, Solving unsymmetric sparse systems of linear equations with PARDISO, Future Generation Computer Systems 20 (3) (2004) 475–487.

[16] P. Amestoy, I. Duff, J.-Y. L'Excellent, J. Koster, A fully asynchronous multifrontal solver using distributed dynamic scheduling, SIAM Journal on Matrix Analysis and Applications 23 (1) (2001) 15–41.

[17] M. L. Parks, E. De Sturler, G. Mackey, D. D. Johnson, S. Maiti, Recycling Krylov Subspaces for Sequences of Linear Systems, SIAM Journal on Scientific Computing 28 (5) (2006) 1651–1674.